PHYSICAL REVIEW FLUIDS **5**, 044304 (2020)

Instability and transition in an elementary porous medium

Xu Chu,[1,*] Yongxiang Wu,[2] Ulrich Rist,[2] and Bernhard Weigand[1]
[1]*Institute of Aerospace Thermodynamics, University of Stuttgart, Pfaffenwaldring 31, D-70569 Stuttgart, Germany*
[2]*Institute of Aerodynamics and Gas Dynamics, University of Stuttgart, Pfaffenwaldring 21, D-70569 Stuttgart, Germany*

(Received 18 December 2019; accepted 31 March 2020; published 22 April 2020)

Instability and transition in an elementary porous medium are investigated via global linear stability analysis and numerical simulation. The porous medium is presented by a representative elementary volume which consists of a staggered array of square cylinders. The stability analysis indicates the first critical Reynolds number at $\mathrm{Re}_{cr} \approx 84$. Two unstable modes are captured from the linear stability analysis: a two-dimensional oscillatory mode and a three-dimensional stationary mode. A series of analyses based on direct and adjoint methods is conducted on both the unstable modes. The energy analysis shows that lift-up and converging-flow effects are both responsible for the unstable modes. In the numerical simulation, the averaged fluctuation profiles exhibit spatial distributions similar to those of the perturbation kinetic energy from the three-dimensional mode, which confirms the prediction from the stability analysis. In addition, we observe stationary counterrotating streamwise vortices beginning at the subcritical Reynolds number, which is a consequence of lift-up instability.

DOI: 10.1103/PhysRevFluids.5.044304

I. INTRODUCTION

Instability and transition in porous media have been barely addressed in the past. Most of the studies dealing with macroscopic modeling and analysis of flow through porous media dealt with creeping and laminar flows. One of the reasons for this might be their relevance in flow through soil, where the velocities are comparably low. On the other hand, there are many applications with porous structures today, where the flow inside the porous structure is in the transitional regime and beyond, e.g., if porous media are used for sophisticated cooling systems [1]. Understanding the instability mechanisms behind laminar-turbulent transitions remains significant in physics and industrial applications. In the current study, microscale-resolving numerical analyses are conducted to understand this important phenomenon in detail. Both numerical simulation and global linear stability analysis are performed to demonstrate the instability mechanism when the Reynolds number $\mathrm{Re} = U_{\mathrm{int}} d/\nu$ increases progressively, where $U_{\mathrm{int}} = \int U dV/V$, d, and ν denote volume-averaged interstitial velocity in the streamwise direction, characteristic length scale inside the porous domain, and kinematic viscosity, respectively.

In nature and industrial applications, porous media can be found at different scales. Selective laser melting, transpiration cooling technology for gas turbine blades, and pebble-bed reactors are some of the applications where porous media are commonly encountered. Geometrical tunability of porous media can be advantageous to control flow characteristics. Darcy [2] defined porous media as "system ensembles of a solid matrix with its void filled with fluids." The interconnected voids

---

[*] xu.chu@itlr.uni-stuttgart.de

allow fluid to flow through the porous medium. Dybbs and Edwards [3] claimed that turbulent flows were observed in experimental studies with a Reynolds number $\mathrm{Re} = U_{\mathrm{int}}d/\nu > 300$. Based on the experiments with laser anemometry and visualization over a wide range of Reynolds numbers, they highlighted the existence of Darcy, steady-laminar inertial, unsteady-laminar, and turbulent regimes. But the exact Reynolds number to classify different flow regimes remains quite controversial [4]. Compared to extensive studies of the low-velocity flow in the Darcy or the laminar regime, the high-velocity flow in the transitional regime and above has been barely investigated. Compared with macroscopic volume-averaged or double-averaged (volume and time) studies, microscopic analysis (resolving the flow field within porous media) has been rarely considered in the past due to its topological complexity. However, there are still some attempts aiming at flow in porous media above the laminar range with flow details resolved at the pore scale.

For a microscopic study of flow through porous media, it is required to resolve the flow field within the porous media. A small representative elementary volume (REV) sample from an infinite cluster of a structured porous medium can reduce the computational burden significantly. Periodic boundary conditions are frequently applied in multiple directions. Hill and Koch [5] conducted their pioneering research on transitional flow in a close-packed face-centered cubic array of spheres via the lattice Boltzmann method (LBM). Their observations suggested that the transition to unsteady flow occurs through a Hopf bifurcation in which only the streamwise velocity starts to fluctuate and the symmetry is broken. They further discussed the transitional flow in wall-bounded porous media [6] which also extended the results in their review article [7]. He *et al.* [8] investigated the same geometry as that of Hill and Koch [5] and increased the Reynolds number to the fully turbulent regime. Multiple Eulerian and Lagrangian statistics were analyzed as a function of Reynolds number. Recently, Agnaou *et al.* [9] investigated the first Hopf bifurcation on 2D periodic ordered and disordered porous structures. The shift of critical Reynolds number with porosity and porous disorder is discussed in depth. They found that the bifurcation is triggered by the oscillation of asymmetric vortices between two successive cylinders along the flow direction. When structural disorder is involved, the critical Reynolds number decreases significantly, which could be explained by the increased tortuosity from the local enlargements and the misalignment of porous structures. Jin *et al.* [10] and Uth *et al.* [11] conducted direct numerical simulation (DNS) in porous media with various topologies to examine the existence of large-scale coherent structures in the turbulent flow regime. It was shown that the pore size restricted the size of large eddies; this is referred to as the "pore-scale prevalence hypothesis." Regarding convective heat transfer in porous structure, Kuwata and Suga [12] and Suga [13] presented large-eddy simulations of pore-scale turbulent flows in porous media via the LBM. Various geometrical morphologies have been considered for modeling. In a previous study, Chu *et al.* [14] simulated fully resolved turbulent flow in regular porous media via DNS, where a link between the macroscopic flow statistics and the corresponding microscopic pore-scale signatures was clearly highlighted.

In the last decades, a few experimental attempts to reveal turbulence characteristics at the microscale were reported [4,15]. Patil and Liburdy [15] designed their porous structure with a randomly packed porous bed and utilized particle image velocimetry for flow field measurements. Coletti *et al.* [16] studied fluid flow and scalar transport through lotus-type porous metals experimentally. The Reynolds number, based on the mean pore diameter and inner velocity, was varied from 80 to 3800. Mayer [1] investigated a metallic porous structure for turbine blade cooling applications. Experiments and simulations were conducted aiming at optimizing the pressure loss and heat transfer. Recently, there has been an increased interest in discovering the detailed fluid physics in the unsteady flow regime in porous media. However, a clear understanding of the laminar-turbulent transitional regime is still lacking. This knowledge could be used further to control the flow or optimize the industrial design.

The complex porous topology leads to a mixture of multiple flow features including shear flow, impinging jets, wakes, and sudden contraction or expansion. Some of these have been observed in both experiments [15] and DNS [14]. In typical sudden contraction or expansion flow scenarios, pitchfork bifurcations are observed as the Reynolds number is increased from zero [17], where the flow bifurcates from a symmetric steady state into an asymmetric steady state [18]. Lashgari *et al.* [17] found a second bifurcation in their study with a planar X junction, which is caused by a three-dimensional stationary global mode. Similarly, a second bifurcation behavior can also be found in flows with roughness elements [19] and in open cavity flows [20].

Global stability analysis, by solving the linearized Navier-Stokes equations, results in a multi-dimensional eigenvalue problem [21]. This is widely used to study flow instability with cylindrical roughness [19], with porous roughness [22], with corner flow [23], with an open cavity [20], and with sudden contraction or expansion [24]. Depending on the local sensitivity, the global modes for sudden-expansion flow [25] and recirculation bubbles [26] are explicitly located either on the far-wake shear or recirculation shear layer. Both studies have shown that the lift-up effect [27], which is effective in turning flow imperfections into streamwise streaks, is the dominating instability mechanism. Due to the non-normality of the linear stability operator [28], transient algebraic increase of the perturbation ahead of the long-term asymptotic behavior as predicted by the linear stability theory can be expected. Tchoufag *et al.* [29] investigated stability and sensitivity of flow past a fixed oblate spheroidal bubble. The lift-up non-normality is substantiated in their direct and adjoint stability analyses. In the non-normal stability study of porous media flow by Rapaka *et al.* [30], they also found the optimal perturbation to be that located at the diffusive zone.

According to the authors' knowledge, global stability analysis has not been carried out for transitional flow in porous media, which motivates this study. In this study, we use global linear stability, structural sensitivity analysis, and numerical simulation to investigate the instability and transition in a porous medium, which could help to close the gap between the studies on traditional Darcy or laminar flow [3] and those on fully developed turbulent flow [8,10,14]. This topological understanding should enable us to suggest targeted flow control by manipulating the porous structures. The present paper is organized as follows. First, we describe the flow configuration, the governing equations for the numerical simulation, and the stability formulations in Sec. II. Then we introduce the numerical methods, solver information, and validation in Sec. III. The results of the stability analysis are presented in Sec. IV, and the observations from the numerical simulation are discussed in Sec. V. Finally, conclusions are given in Sec. VI.

II. NUMERICAL FRAMEWORK

A. Flow configuration and problem formulation

The porous structure studied here is composed of a staggered array of square cylinders, as illustrated in Fig. 1. The unit representative elementary volume (REV) size in the two-dimensional (x-y) plane is $4d \times 2d$, where d is the width of the square cylinders; a computational domain size of $4d \times 4d$ in the x-y plane is used here to capture symmetry breaking with affordable additional computational cost. The flow is imposed in the x direction driven by a pressure gradient. The length of cylinder d and the interstitial velocity U_{int} are used for the nondimensionalization. With the current formulation, the geometry can be considered as a small REV sample from an infinite cluster of a structured porous medium.

B. Governing equations

Numerical simulations involve the solution of the three-dimensional (3D) incompressible Navier-Stokes equations, given by Eqs. (1) and (2), where $\vec{\Pi}$ is the source term in the momentum equation to maintain a constant nonzero mass flux in the x direction:

$$\nabla \cdot \boldsymbol{U} = 0, \tag{1}$$

$$\frac{\partial \boldsymbol{U}}{\partial t} + (\boldsymbol{U} \cdot \nabla)\boldsymbol{U} = -\nabla P + \frac{1}{\text{Re}}\Delta \boldsymbol{U} + \vec{\Pi}, \tag{2}$$

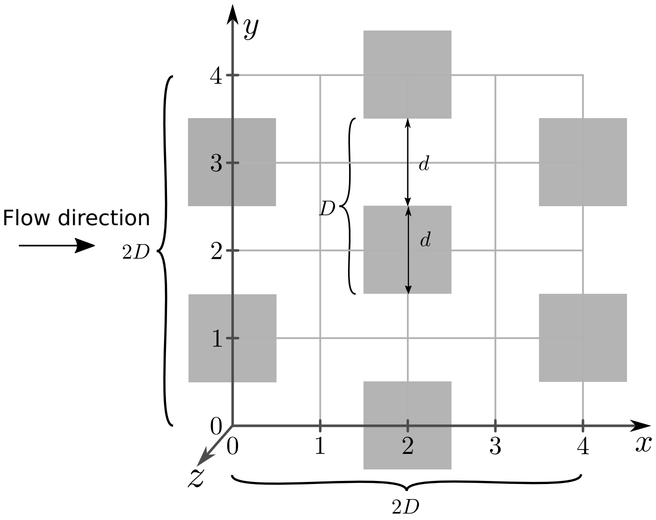

FIG. 1. A two-dimensional sketch of the three-dimensional simulation domain with the homogeneous direction z; d indicates the width of square cylinder and void. The simulation domain is defined by the region $0 \leqslant x \leqslant 4$, $0 \leqslant y \leqslant 4$, and $0 \leqslant z \leqslant 4$.

where $\boldsymbol{U} = (U, V, W)$ is the vector of the velocity components in the reference system of (x, y, z) and P the pressure term. The length and velocity are dimensionless with respect to square cylinder width d and the volume-averaged interstitial velocity in the x direction U_{int}. The Reynolds number Re is defined as

$$\text{Re} = \frac{U_{\text{int}} d}{\nu}, \tag{3}$$

with ν being kinematic viscosity. For the three-dimensional numerical simulations, periodic boundary conditions are imposed at the streamwise boundaries ($x = 0$ and $x = 4$), the lateral boundaries ($y = 0$ and $y = 4$), and spanwise boundaries ($z = 0$ and $z = 4$). On all the walls of the square cylinders, no-slip and no-penetration boundary conditions ($\boldsymbol{U} = 0$) are given.

C. Base flow computation and linear stability analysis

In order to perform a linear stability analysis, we decompose the flow into a two-dimensional steady-state base flow and an infinitesimal three-dimensional unsteady perturbation. The velocities and pressure from base flow and perturbation are denoted by $Q = (\boldsymbol{U}_b, P_b)$ and $q = (\boldsymbol{u}, p)$, respectively. Obtaining the base flow is a critical issue for linear stability analysis. In the case of spatially developing X-junction flow, Lashgari *et al.* [17] computed the base flow with a half-domain size to ensure axisymmetry for the first bifurcation condition, whereas the base flow for the second bifurcation is asymmetric. This follows the classical approach used in the studies of a wake behind a bluff body [31]. In the current study, base flow computation is enabled via the implementation of the selective frequency damping (SFD) function (as described in Åkervik *et al.* [32]) into the governing equations (1) and (2) with an additional equation for the temporally filtered state $\overline{\boldsymbol{U}}$. This implementation enables a damping of the oscillations of the unsteady part of the solution using a temporal low-pass filter. This is achieved by adding a forcing term to the right-hand side of the momentum equation (2), which leads to

$$\nabla \cdot \boldsymbol{U} = 0, \tag{4}$$

$$\frac{\partial \boldsymbol{U}}{\partial t} + (\boldsymbol{U} \cdot \nabla)\boldsymbol{U} = -\nabla p + \frac{1}{\mathrm{Re}}\Delta \boldsymbol{U} + \vec{\Pi} - \chi(\boldsymbol{U} - \overline{\boldsymbol{U}}), \tag{5}$$

$$\frac{\partial \overline{\boldsymbol{U}}}{\partial t} = \omega_c(\boldsymbol{U} - \overline{\boldsymbol{U}}), \tag{6}$$

where the cutoff frequency ω_c and control coefficient χ are adjusted empirically for achieving convergence to steady state. The SFD method makes use of splitting methods, which enables it to be built on the existing code. The effort to implement a steady-state solver into an existing unsteady code is thus reduced. However, it should be noted that SFD is not able to quench pitchfork type bifurcation with zero frequency. To obtain the steady base flow, periodic boundary conditions are imposed at the inlet ($x = 0$) and outlet ($x = 4$), and lower boundary ($y = 0$) and upper boundary ($y = 4$), where the no-slip boundary condition is applied on the surfaces of square cylinders. With the SFD method, Eqs. (4)–(6) converge toward the steady-state solution $\boldsymbol{U}_b$ to perform linear stability analysis.

The linearized Navier-Stokes equations read

$$\nabla \cdot u = 0, \tag{7}$$

$$\frac{\partial \boldsymbol{u}}{\partial t} + \boldsymbol{u} \cdot \nabla \boldsymbol{U}_b + \boldsymbol{U}_b \cdot \nabla \boldsymbol{u} = -\nabla p + \frac{1}{\mathrm{Re}}\nabla^2 \boldsymbol{u}. \tag{8}$$

The perturbation state vector q takes the form of two-dimensional global modes, which is commonly known as the BiGlobal stability analysis [21]:

$$\boldsymbol{u}(x, y, z, t) = \hat{\boldsymbol{u}}(x, y)e^{\lambda t + i\beta z}, \tag{9}$$

$$p(x, y, z, t) = \hat{p}(x, y)e^{\lambda t + i\beta z}, \tag{10}$$

where β is the wave number of the perturbation flow in the z direction. For a given β, the complex frequency, $\lambda = \sigma + i\omega$, can be computed by solving the eigenvalue problem resulting from the perturbation equations.

The real σ and imaginary ω parts of the eigenvalue λ are the growth rate and oscillation frequency of the corresponding global mode, respectively. If there exists any eigenvalue with positive real part ($\sigma > 0$), the flow is linearly unstable. Conversely, if all eigenvalues have $\sigma < 0$, the flow is linearly stable and infinitesimal perturbations eventually decay to zero. To solve the linearized Navier-Stokes equations, periodic boundary conditions are imposed at the inlet ($x = 0$) and outlet ($x = 4$), and lower boundary ($y = 0$) and upper boundary ($y = 4$).

D. Adjoint stability formulation

Adjoint global modes are calculated to construct the structural sensitivity, which identifies the core region of the instability, defined as the region where a local feedback force proportional to the velocity results in the largest drift of the leading eigenvalue [33,34]. Here, we introduce a similar ansatz for the adjoint system:

$$\boldsymbol{u}^{\dagger}(x, y, z, t) = \hat{\boldsymbol{u}}^{\dagger}(x, y)e^{\lambda^{\dagger} t - i\beta z}, \tag{11}$$

$$p^{\dagger}(x, y, z, t) = \hat{p}^{\dagger}(x, y)e^{\lambda^{\dagger} t - i\beta z}, \tag{12}$$

where $\boldsymbol{u}^{\dagger} = (u^{\dagger}, v^{\dagger}, w^{\dagger})$ and $p^{\dagger}$ are defined as the adjoint velocity and pressure perturbation fields. Therefore, the adjoint stability problem is formulated as

$$\nabla \cdot \boldsymbol{u}^{\dagger} = 0, \tag{13}$$

$$-\frac{\partial \boldsymbol{u}^{\dagger}}{\partial t} - \nabla \boldsymbol{U}_b \cdot \boldsymbol{u}^{\dagger} + \boldsymbol{U}_b \cdot \nabla \boldsymbol{u}^{\dagger} = -\nabla p^{\dagger} + \frac{1}{\mathrm{Re}} \nabla^2 \boldsymbol{u}^{\dagger}. \tag{14}$$

For more information about the derivation of the adjoint equations, one can refer to Barkley *et al.* [35], Blackburn *et al.* [36], or the recent review article by Luchini and Bottaro [34].

E. Perturbation energy analysis

Further investigation of the instability mechanisms and where these unstable global modes extract their energy from the base flow is important. To answer this question, the budget of perturbation kinetic energy from the Reynolds-Orr equation reads

$$\frac{\partial E}{\partial t} = \int I_i dV - \int D dV, \tag{15}$$

where $E = 0.5 \int (u^2 + v^2 + w^2) dV$ and $D = \frac{1}{\mathrm{Re}} \nabla u \cdot \nabla u$ are the volume-averaged perturbation kinetic energy and dissipation terms, respectively. The production terms I_i are written as

$$\begin{aligned} I_1 &= -uu\frac{\partial U_b}{\partial x}, \quad I_2 = -uv\frac{\partial U_b}{\partial y}, \\ I_3 &= -vu\frac{\partial V_b}{\partial x}, \quad I_4 = -vv\frac{\partial V_b}{\partial y}. \end{aligned} \tag{16}$$

Calculating this kinetic energy transfer provides insights into the spatial stabilizer and destabilizer. Different physical mechanisms are related to these four contributions I_{1-4} [Eq. (16)]. For instance, the term $I_2 = -uv\partial U_b/\partial y$, involving the gradient of base-flow streamwise velocity in the lateral direction y, is associated with the lift-up mechanism. The term $I_1 = -uu\partial U_b/\partial x$, involving the gradient of base-flow streamwise velocity in the streamwise direction, is an indication of the contribution from flow acceleration and deceleration through the converging and diverging channel network. The last term I_4 consists of the lateral perturbation energy vv and the lateral gradient of the base flow velocity in that direction $\partial V_b/\partial y$. This is relevant to the flow converging-diverging mechanism. The signs of the different terms I_i indicate that the associated physical mechanisms either quench (negative) or promote (positive) the considered instability.

III. NUMERICAL METHOD

A. Numerical simulation

The governing equations are discretized and solved via two individual numerical solvers, a finite-volume solver in OpenFOAM [37] and a spectral/*hp* element solver in Nektar++ [38,39]. In the solver based on the finite-volume method (FVM), the spatial discretization is performed with a central differencing scheme, whereas the temporal discretization is through a second-order implicit Euler scheme. The pressure implicit with splitting of operators (PISO) algorithm is employed for pressure-velocity coupling in a semi-implicit way. The Poisson equation for the pressure is iteratively solved with a geometric-algebraic multigrid approach. The source term $\vec{\Pi}$ is adjusted dynamically in each time step to ensure a constant mass flux in the entire domain, which corresponds to a constant U_{int} at each time step. Although the corresponding pressure gradient is not strictly constant in time, it fluctuates no more than 1% with respect to the mean value, once a statistically steady state is achieved. The algorithm is second-order accurate in space and time. The solver is parallelized with a pure message passing interface. A mesh resolution of $72\,960 \times 240$ ($xy \times z$;

17.5 million cells in total) is used for all the considered Reynolds numbers. The nondimensional time step is fixed at $\Delta t/(d/U_{\mathrm{int}}) = 0.001$.

The numerical simulation is also conducted with a spectral/*hp* element solver Nektar++ [38,39]. The solver framework allows arbitrary-order spectral/*hp* element discretizations with hybrid shaped elements. In addition, the homogeneous flow direction can be represented with spectral expansions. The spectral-accurate discretization combined with meshing flexibility is well suited to deal with complex geometry. The porous medium geometry, introduced in Sec. II A, is discretized with full quadrilateral elements in the x-y plane with local refinement, where 8th-order Lagrange polynomials through the nodal Gauss-Lobatto-Legendre base (GLL spectral-element method, SEM) are applied. The third direction (z direction) is discretized with a Fourier-based spectral method. The 810 quadrilateral elements using 8th-order Lagrange polynomial discretization combined with 144 Fourier modes in the z direction leads to a resolution of 7.5×10^6 degrees of freedom, which is used in all numerical simulation cases. Although this resolution was initially planned for a higher Reynolds number flow range, it is fixed for all the considered numerical simulation cases to reduce the meshing burden. The time-stepping is treated with a second-order mixed implicit-explicit (IMEX) scheme. The dimensionless time step is fixed at $\Delta t/(d/U_{\mathrm{int}}) = 0.0005$. The flow is driven by a constant pressure gradient, which is identical to the time-averaged pressure gradient in the FVM solver. The initial velocity field was random. All numerical simulations were run on the Cray XC40 cluster Hazel Hen at HLRS (National High Performance Computing Center) located in Stuttgart, Germany.

B. Base flow and linearized solver

For the direct and adjoint stability analyses, it is necessary to specify a base flow for each Reynolds number. The base flow is computed using the same spectral/*hp* element solver. Local discretization in the element is achieved with modified Gauss-Legendre polynomials [40] following $\mathbb{P} - \mathbb{P}_{N-2}$ formulation with 8th-order accuracy ($P = 8$). The pressure gradient identical to the numerical simulation setting is applied on the base flow equation to achieve an approximately identical Reynolds number. A time-stepping technique is used to calculate the evolution of the direct and adjoint equations [35,41]. The analysis is based on a Krylov-subspace iteration of successive finite increments of initially random perturbations through the linearized Eqs. (7) and (8) using an Arnoldi method (ARPACK library based) to extract the dominant eigenpairs of the exponential operators. The size of the Krylov space dimension used by the Arnoldi algorithm is 64. We would like to remark that no shift parameter has been used for these calculations. The convergence is examined by progressively increasing the size of Krylov subspaces to 128 and 256. The tolerance applied to the Arnoldi iteration residual (see Sherwin and Blackburn [42]) as a stopping criterion was 1×10^{-6}.

The adjoint equations [Eqs. (11) and (12)] can be solved with an algorithm similar to that for the direct equations, which is commonly named the continuous-adjoint method. The other possibility is the discrete-adjoint method, which discretizes the continuous equations, and then writes the adjoint of the discretized system. According to the comparison by Chandler *et al.* [43], both paths find the same eigenvalue of the most unstable global mode. However, the continuous strategy requires less resolution and usually converges faster than the discrete-adjoint approach.

C. Validation

Cautious validations are carried out for both linear stability analysis and numerical simulations. A microscopic validation of numerical simulation results is also performed by comparing two solvers together with polynomial refinement, which can be found in the Appendix. Here, we show the effect of the resolution on finding the least stable mode from the stability analysis. Through this, we ensure that the leading eigenvalue does not vary when the spatial resolution is increased. Table I lists leading eigenvalue pairs at Reynolds numbers $\mathrm{Re} = 70$ and $\mathrm{Re} = 100$ for which the flow is stable and unstable, respectively. Progressively increasing the polynomial order from $P = 6$ to $P = 11$

TABLE I. Comparison of leading eigenvalues of direct and adjoint linearized Navier-Stokes operators at different polynomial refinements.

Case	$P = 6$	$P = 8$	$P = 11$
Re = 70	$-0.2189 \pm 2.6546i$	$-0.2195 \pm 2.6543i$	$-0.2198 \pm 2.6541i$
Re = 100	$0.1699 \pm 4.2941i$	$0.1691 \pm 4.2945i$	$0.1687 \pm 4.2945i$
Re = 100 (Adjoint mode)	$0.1702 \pm 4.2940i$	$0.1693 \pm 4.2935i$	$0.1688 \pm 4.2931i$

results in minimal change of leading eigenvalues after the third or fourth decimal place, which is an indication of numerical convergence. Furthermore, the direct eigenvalues and adjoint eigenvalues calculated at Re = 100 are almost identical at each mesh resolution.

IV. LINEAR STABILITY ANALYSIS

A. Base flow

Figure 2 depicts the distribution of streamwise velocity U_b of the base flow for the Reynolds numbers Re = 10, 90, 110. Black contour lines are contours of constant U_b with $U_b < 0$ ($-0.26 \leqslant U_b \leqslant -0.01$ with a contour level of 0.05). At Re = 10 [Fig. 2(a)], the symmetrical streamlines (in red) are approximately attached to the solid surfaces and converge in the center of the next channel. In the rest of the Re cases, streamlines cover two separation bubbles on the lateral shear walls and a large recirculation bubble in the wake. At the lowest Reynolds number [Re = 10; Fig. 2(a)], high velocity is observed in the center of the streamwise channels, whereas low velocities are present close to the impinging and wake surfaces. The lateral separation bubbles are not detected in the base flow due to weak inertial effects. Therefore, the streamlines stick to the solid surfaces. The recirculation area behind the bluff body is observed with a negative U_b region of small magnitude. At Re = 90, a pair of symmetric boundary layers (dark purple tone) in the streamwise channels is identified, which is not seen in Fig. 2(a). A significant flow separation around the sharp corners leads to the formation of lateral bubbles presented by black contours. Large recirculation bubbles are hidden in the wake areas of the bluff bodies and surrounded by the red streamlines. This appears usually with the flow over bluff bodies. Both types of bubbles and related instability issues have been reported in the literature. Such separation bubbles are seen in flow over forward- and backward-facing steps [36], flow through converging-diverging channels [44], and X-junction flows [17].

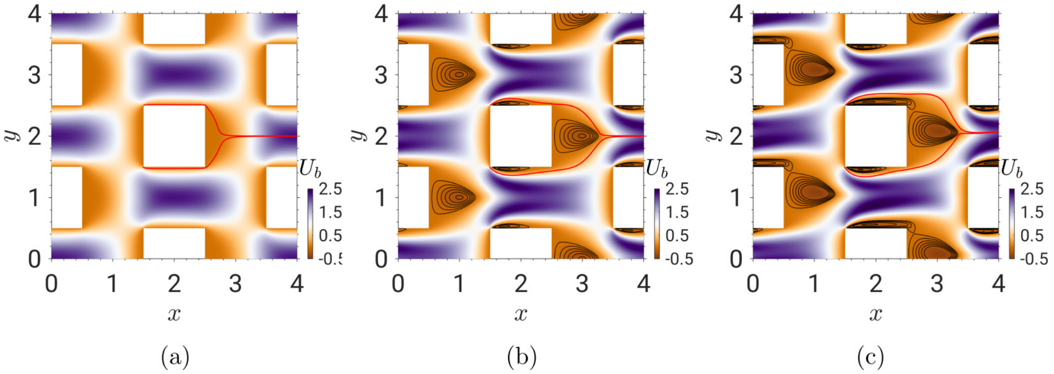

(a)

(b)

(c)

FIG. 2. Spatial distribution of base flow velocity in streamwise direction U_b. Contours in black describe negative U_b areas ($-0.26 \leqslant U_b \leqslant -0.01$); streamlines in red describe flow starting from sharp corners, which covers the recirculation bubbles on the shear walls and the large recirculation bubble in the wake, except for Re = 10. (a) Re = 10. (b) Re = 90. (c) Re = 110.

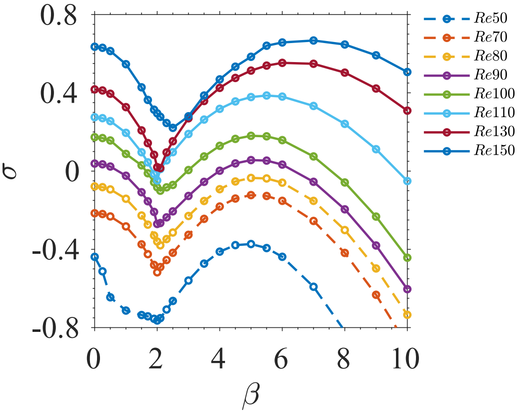

FIG. 3. Leading growth rate σ as a function of spanwise wave number β. Reynolds number ranges from $\mathrm{Re} = 50$ to $\mathrm{Re} = 150$.

On further increasing the Reynolds number to 110 [Fig. 2(c)], the two streamlines and the small separation bubble pairs lose their mirror symmetry with respect to $y = \pm n, n \in \mathbb{N}$. The high-velocity stream bulk (in purple) tilts to the upper side. The two recirculation regions have unequal sizes: a smaller one on the tilted side and a larger one on the other side. The attachment of a jet flow to the adjacent wall refers to the Coanda effect, which has been also observed in the X-junction flow [17].

B. Linear stability analysis

Based on the steady-state base flows, the results from linear stability analysis are analyzed in this subsection to reveal the most dangerous mode. Figure 3 depicts the growth rate σ of the leading global mode as a function of spanwise wave number β. A fine scan of spanwise wave numbers $\beta = 0$, 0.25, 0.5, 1, 1.5, 1.7, 1.9, 2, 2.1, 2.3, 2.5, 3, 3.5, 4, 4.5, 5, 5.5, 6, 7, 8, 9, 10, 15, 20 is considered for a series of Reynolds numbers: $\mathrm{Re} = 50$, 70, 80, 90, 100, 110, 130, 150. The growth rates at $\beta \geqslant 10$ show a monotonically rapid decrease. Therefore it is to be concluded that the computed wave number range is large enough to investigate the most dominant instability and to omit the results for $\beta \geqslant 10$. Figure 3 indicates significant dual peaks in the range of Reynolds number considered here. Local minima of the growth rate are observed at $\beta \approx 2$. A maximum in leading growth rate occurs at $\beta = 0$, whereas the other is observed at a higher wave number, which increases from $\beta = 5$ at lower Reynolds number ($\mathrm{Re} = 50$–90) to $\beta = 7$ at $\mathrm{Re} = 150$. The zero spanwise wave number suggests that this leading mode is two-dimensional, whereas the other one is clearly three-dimensional. Both unstable modes exhibit comparable growth rates for the same Reynolds number pointing to the dominance of both of these modes. The critical Reynolds number, at which the flow becomes unstable, lies between $\mathrm{Re} = 80$ ($\sigma = -0.03503$ at $\beta = 5$) and $\mathrm{Re} = 90$ ($\sigma = 0.05611$ at $\beta = 5$). A linear interpolation from these growth rates at $\beta = 5$ leads to a prediction of critical Reynolds number $\mathrm{Re}_{cr1}^{LST} \approx 84$, where the same procedure for $\beta = 0$ results in another critical Reynolds number of $\mathrm{Re}_{cr2}^{LST} \approx 87$.

The eigenvalue spectra from $\mathrm{Re} = 80$ to $\mathrm{Re} = 110$ at $\beta = 0$ and $\beta = 5$ are shown in Fig. 4. The distribution of the eigenvalues is symmetrical along the zero abscissa. All eigenmodes are stable (negative growth rate) at $\mathrm{Re} = 80$ (blue circles) for both $\beta = 0$ and $\beta = 5$. In Fig. 4(a), the two-dimensional oscillatory mode at $\mathrm{Re} = 90$ shows an oscillation frequency $\omega = \pm 2.6454$. At $\mathrm{Re} = 100 > \mathrm{Re}_{cr1,2}$, the mode emerging from the critical mode is not the fastest growing mode. In other words, the mode with the largest growth rate changes. In Fig. 4(b), the leading unstable modes, at the three cases of Reynolds numbers where this is observed, exhibit zero oscillation frequency. Thus, this dangerous mode is a three-dimensional steady mode.

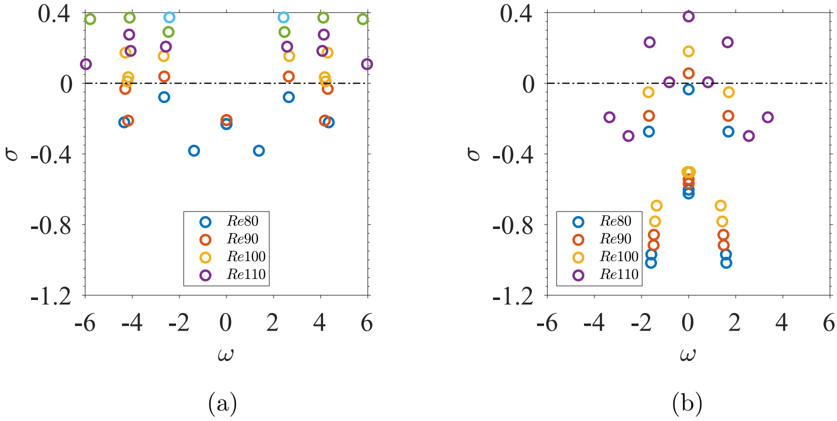

FIG. 4. Eigenvalue spectra of $\mathrm{Re} = 80, 90, 100, 110$. (a) Spanwise wave number $\beta = 0$. (b) Spanwise wave number $\beta = 5$.

The leading growth rate and eigenvalue spectra suggest the significance and difference between the two-dimensional instability at $\beta = 0$ and three-dimensional instability at $\beta \approx 5$. They will be analyzed and discussed separately in the following sections.

C. Two-dimensional unstable mode at $\beta = 0$

1. *Direct stability analysis*

The spatial distribution of the direct ($\lambda = 0.0383 + 2.6433i$) and adjoint eigenmode at the unstable Reynolds number $\mathrm{Re} = 90$ is shown in Fig. 5 with streamlines. Although the porous medium has a morphology similar to that of the X-junction flow in Lashgari *et al.* [17], the spatial distribution of the unstable global mode is more complicated. In Lashgari *et al.* [17], the instability is first observed after the lateral flows merge into the streamwise channel (after $x = 1$ in Fig. 2 of Lashgari *et al.* [17]). In this elementary porous medium, the instability is distributed periodically in the simulation domain. It can also be interpreted that in the X-junction flow, the strongest perturbation is only found in the convergent flow section, whereas in the present porous medium

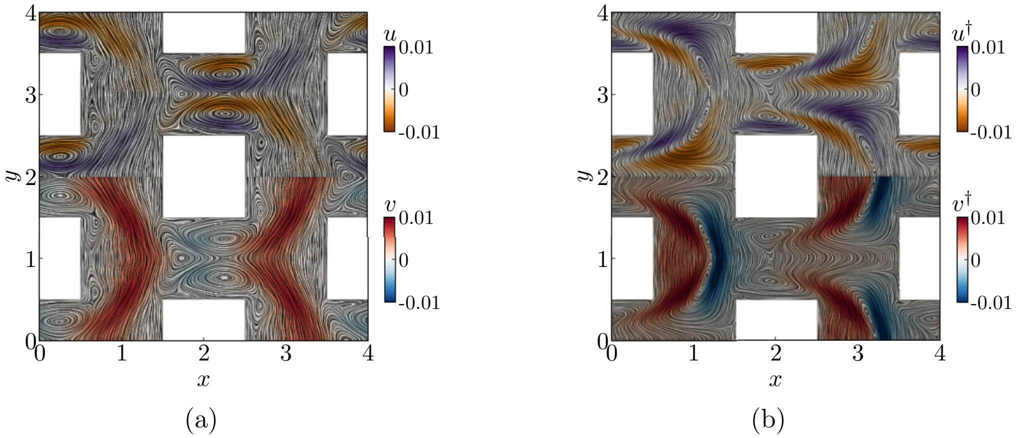

FIG. 5. Spatial distribution of two-dimensional direct and adjoint modes at $\mathrm{Re} = 90$. (a) Streamlines from the perturbation field u and v. (b) Streamlines from the adjoint field $u^\dagger$ and $v^\dagger$.

the strongest perturbation is found at both convergent and divergent flow sections. This complex instability warrants a careful investigation.

The streamlines in Fig. 5(a) exhibit vortices at the converging inlet (vortex center at $x \approx 1.5$) followed by pairs of mirror-symmetry vortices with respect to $y = \pm n, n \in \mathbb{N}$. In the upper side, the perturbation velocity field u is antisymmetric with respect to $y = \pm n, n \in \mathbb{N}$. Two types of prevalent structures are observed surrounding the vorticity pairs: the larger one starts from the sharp corners [for instance, $(x, y) = (1.5, 2.5)$], lifts up, and then converges in the next channel. The smaller one is sandwiched between the large perturbation structures and solid walls. The magnitude of the lateral component v [lower side of Fig. 5(a)] is quite comparable to that of u, which differs from the weak lateral perturbation (one order of magnitude lower than streamwise perturbation) in the X-junction flow (Fig. 4 in Lashgari *et al.* [17]). This indicates clearly that the lateral instability is as important as the streamwise one in this REV of a porous medium. The v perturbation shows two types of structures: the most obvious large-scale structures appear in the lateral channels (continuous void in the y direction) and interconnected with each other in the y direction. The smaller structures with lower amplitude lie in the streamwise channels.

2. *Adjoint stability analysis*

Adjoint stability analysis is enabled by the continuous strategy in the computation. Streamlines in Fig. 5(b) indicate pairs of vortices in the shear channels ($x \approx 1.8$), induced by high magnitude of $u^\dagger$. The adjoint global mode shows different distribution from the direct global mode in Fig. 5(a). Streamwise perturbation velocity $u^\dagger$ [Fig. 5(b)] exhibits its dominant structures close to the diverging flow region, for example $(x, y) = (3, 2.8)$. Lateral perturbation velocity $v^\dagger$ shows two successive structures in the wake region. The dominant $u^\dagger$ and $v^\dagger$ structures lead to flat vorticity pairs in the wake.

3. *Perturbation kinetic energy*

From the direct and adjoint stability analysis above, it can be noted that both streamwise and lateral perturbations have a crucial effect on the unstable modes. It makes sense to investigate the perturbation kinetic energy (PKE) from the direct mode $E = 1/2(u^2 + v^2 + w^2)$ and from the adjoint mode $E^\dagger = 1/2(u^{\dagger,2} + v^{\dagger,2} + w^{\dagger,2})$. It shall be noted that the magnitude of the spanwise component is much weaker than the other two. A spatial description of PKE of the leading direct and adjoint global modes is given in Fig. 6. It should be noted that the spanwise component is negligible on this shown cutting plane. In Fig. 6(a), maximal perturbation energy is observed as a pair at the free hyperbolic stagnation points of the base flow (approximately $x \approx 1$ or $x \approx 3$). The distribution of E is symmetric with respect to $y = \pm n, n \in \mathbb{N}$. This pair of high-energy spots are allocated on lateral sides of the merging red streamlines [see $(x, y) = (3, 1.5)$]. Other secondary energy spots are found in the streamwise shear channels. PKE from the adjoint mode is depicted in Fig. 6(b). The most significant feature is found on the top of the recirculation bubble in the wake, and the secondary feature underlying on the lateral sides of the recirculation bubble. The PKE from both direct mode and adjoint mode at $\mathrm{Re} = 90$ indicates strong instability in the lateral channels. Special attention should be paid to the wake region with converging and diverging flow regions. Multiple energetic structures are found surrounding the recirculation bubbles, for instance on the sides and on its top.

In the remaining panels of Fig. 6, the associated perturbation kinetic energies in the streamwise direction and lateral direction from the direct mode (E_{uu} and E_{vv}) and the adjoint mode ($E^\dagger_{uu}$ and $E^\dagger_{vv}$) are described. PKE in the streamwise direction E_{uu} [Fig. 6(c)] is intense essentially within the confined channels. Lateral perturbation energy E_{vv} [Fig. 6(d)] exhibits a significant magnitude in the upstream direction of the channel inlets, where lateral flows merge with each other. Clearly, the magnitude of E_{vv} exceeds that of E_{uu} and therefore contributes to the PKE distribution in Fig. 6(a) largely. The magnitude of the adjoint modes [Figs. 6(e) and 6(f)] is not quite comparable to that of the direct mode. Lateral kinetic energy $E^\dagger_{vv}$ shows higher strength than the streamwise component

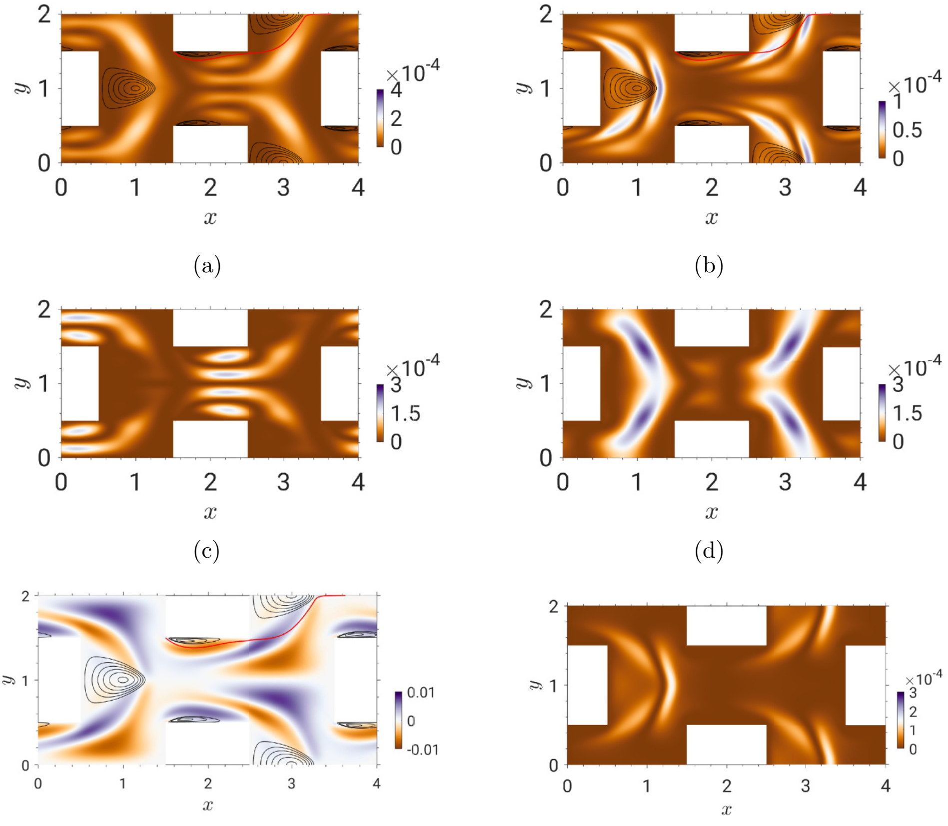

(a)

(b)

(c)

(d)

(e)

(f)

FIG. 6. Spatial distribution of perturbation kinetic energy of leading direct mode and adjoint mode at Re $=$ 90. Bubble contours in black and streamlines in red are the same as in base flow, as in Fig. 2. Half of the domain is shown to maintain simplicity. (a) PKE from the direct mode. (b) PKE from the adjoint mode. (c) E_{uu} from the direct mode. (d) E_{vv} from the direct mode. (e) $E_{uu}^{\dagger}$ from the adjoint mode. (f) $E_{vv}^{\dagger}$ from the adjoint mode.

$E_{uu}^{\dagger}$. The most noticeable maximum of $E_{vv}^{\dagger}$ corresponds to both the wake area and the merging flow at the channel inlet. This dominant lateral modal energy is usually referred to as lift-up non-normality [29].

The energy analysis introduced in Sec. II E is suited for a further investigation. The spatial distribution of the energy transfer can provide insight into the physical instability mechanism [25]. The spatially integrated production and dissipation terms, normalized with $\int D dV$ at stable Reynolds number Re $=80$ and unstable Re $=90$, are summarized in Fig. 7. At both Reynolds numbers, I_2 and I_4 are dominant terms for the production. At Re $=80$, both I_2 and I_4 are weaker than the dissipation ($I_{2,4} < D$). The converging-diverging production I_4 is the most significant contributor. As Reynolds number increases, the leading place of I_4 is replaced by lift-up production I_2. The transition progress seems to be accompanied by the growing lift-up mechanism, whereas the converging-diverging mechanism plays a secondary role.

An investigation into the spatial distribution of the total production $\sum I_i$ on the leading direct global mode is shown in Fig. 8. At the first Reynolds number above the critical one (Re $=90$), the total production distribution [in Fig. 8(a)] exhibits a strong similarity to the perturbation kinetic energy in Fig. 6(a). A pair of symmetrical maxima is observed at the converging channel inlet. The second peak arises from the separation flow around sharp corners following the base

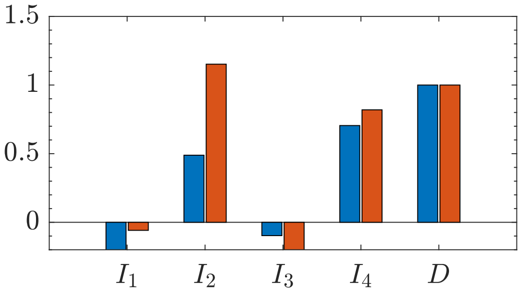

FIG. 7. Perturbation kinetic energy terms $\int I_i dV$, normalized by the dissipation $\int D dV$. The blue and red bars correspond respectively to Re $= 80$ and Re $= 90$.

flow streamlines, lying outside of the separation bubbles. This smaller peak is similar to the first bifurcation in the X-junction flow [17]. However, the most dominant pair is found only in the porous media studied here. It reveals that the first bifurcation is provoked by the instability of two flows encountered in a converging channel.

Furthermore, the spatial distribution of decomposed components—lift-up production I_2 and converging-diverging production I_4—are depicted in Figs. 8(b) and 8(c). Both I_2 and I_4 promote the instability surrounding the recirculation bubble, e.g., at $x = 1$. However, the maximum of I_2 is located upstream of the location at which I_4 has its maximum. Spatially, the most significant production I_2 is found around the diverging flow region, due to a strong velocity gradient. In Fig. 8(c), converging-diverging production I_4 is located in the converging flow position, which is the consequence of significant vv and $\partial V_b/\partial y$ in this position. It can be concluded that lift-up

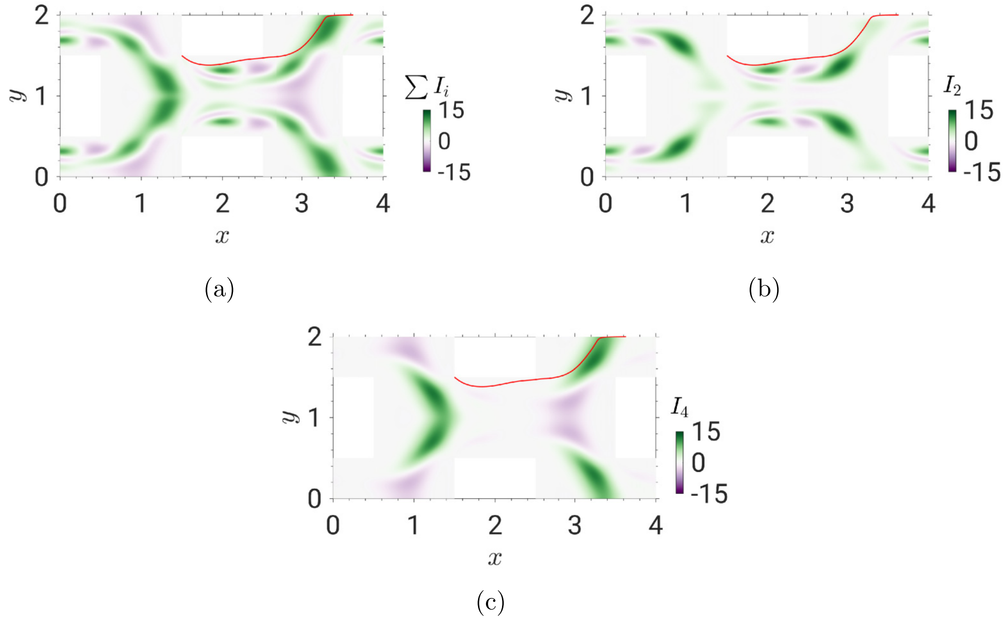

(a)

(b)

(c)

FIG. 8. Spatial distribution of production terms of perturbation kinetic energy of the leading direct global mode at Re $= 90$. (a) Total production $\sum I_i$. (b) Lift-up production I_2. (c) Converging and diverging production I_4.

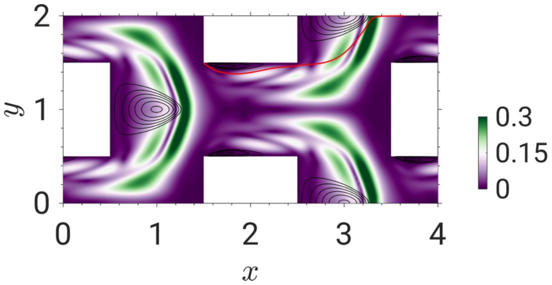

FIG. 9. Sensitivity analysis ζ distribution. Bubble contours in black and streamlines in red are the same as in base flow at $\mathrm{Re} = 90$.

production I_2 is mainly contributed by the strong shear in the streamwise channels and the diverging flows, whereas the I_4 is closely related to the converging flow at the channel entry.

4. *Sensitivity analysis*

The perturbation kinetic energy budget provided a better understanding of the energy balance for the instability mechanisms. The concept of sensitivity analysis measures the sensitivity of the growth rates to localized perturbations. The methodology was introduced by Giannetti and Luchini [33] where it has been applied to the global instability of a flow around a cylinder. It enables one to identify the most likely region for the receptivity of the global instability under consideration, which is also referred to as structural sensitivity. Following the definition by Giannetti and Luchini [33], the measurement of sensitivity is given as the product of the direct and adjoint modes:

$$\zeta(x,y) = \frac{\parallel \boldsymbol{u}^{\dagger}(x,y) \parallel \parallel \boldsymbol{u}(x,y) \parallel}{\int \boldsymbol{u}^{\dagger} \cdot \boldsymbol{u} dA}. \tag{17}$$

In Fig. 9, a significant continuous curvy structure is observed, starting from the diverging flow region in the upstream to the converging flow region in the downstream. The maxima are located at where lateral streams start to converge, e.g., on the top of the recirculation bubble. This is clearly described by the trace of both streamlines and consistent with the perturbation kinetic energy in Fig. 6(a) and the total production in Fig. 8(a). In a cylinder wake flow [29,33], the recirculation region is considered as the origin of instability showing a pair of lateral wave makers. It is also relevant to the sinuous instability in a cylinder-mounted boundary layer transition [19]. Here in porous media, the wake is frequently associated with other flow regimes such as converging or impinging, which leads to a higher complexity of the sensitive topology.

D. Three-dimensional instability at $\beta = 5$

The growth rate in Fig. 3 indicates another significant mode at spanwise wave number $\beta \approx 5$. Unlike the two-dimensional mode at $\beta = 0$, this mode is three-dimensional ($\beta \neq 0$) and stationary. Figure 10 reveals streamlines of the direct and adjoint mode at $\beta = 5$ for $\mathrm{Re} = 90$ on the nodal plane $z = 0$, where the maxima of energy production is observed. The streamlines are colored with the different velocity components. Streamwise perturbation velocity u in Fig. 10(a) exhibits large-scale structures starting from the corners of the channel entry and ending with a mild impinging on the next porous unit. This impinging also produces vortical structures close to the solid surfaces (say $x \approx 3.2$). The lateral perturbation component v has a slightly weaker but still comparable amplitude. Its topology is rather simple, which is a large continuous structure filled within one straight channel void (for instance between $x = 1$–3 and $y = 0.5$–1.5). This topological appearance is quite different from the one observed at $\beta = 0$ in Fig. 5(a).

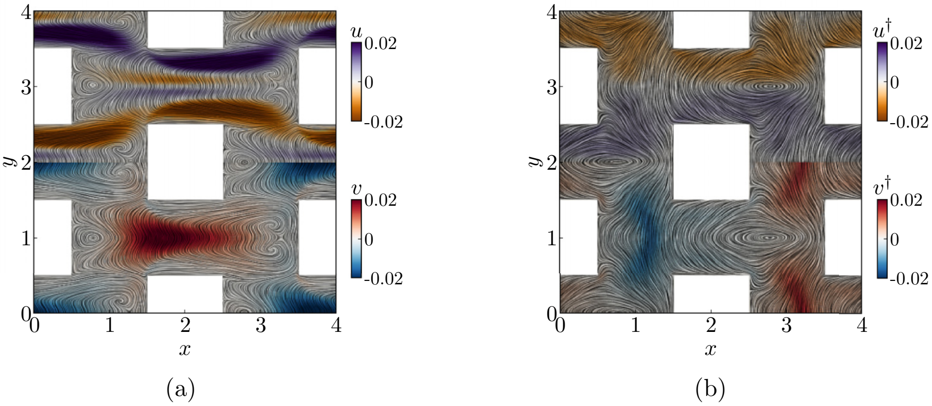

FIG. 10. Three-dimensional direct and adjoint mode at $\beta = 5$ for Re $= 90$ on the plane $z = 0$. (a) Streamlines from the perturbation field u and v. (b) Streamlines from the adjoint field $u^\dagger$ and $v^\dagger$.

The adjoint mode at $\beta = 5$ for Re $= 90$ is described in Fig. 10(b). Its appearance is quite distinguishable from the direct mode. Streamwise perturbation velocity $u^\dagger$ is antisymmetric with respect to $y = \pm n, n \in \mathbb{N}$. Lateral perturbation $v^\dagger$ exhibits its significance mainly in the lateral channels.

Analogous to the approach in the two-dimensional unstable mode ($\beta = 0$), the distributions of kinetic energy in streamwise direction E_{uu} and lateral direction E_{vv} are depicted in Figs. 11(a) and 11(b); both are the components of total kinetic energy. E_{uu} shows long and continuous structures on lateral sides of the solid surfaces, which corresponds to a typical fluctuation energy in the case of flow across bluff bodies. Lateral perturbation kinetic energy E_{vv} in Fig. 11(b) shows high-energy spots corresponding to the merged flows within streamwise parallel channels. The spatial energy distributions of $E^\dagger_{uu}$ and $E^\dagger_{vv}$ from the adjoint mode are described in Figs. 11(c) and 11(d). Unlike those from the direct mode [Figs. 11(a) and 11(b)], lateral energy $E^\dagger_{vv}$ shows a much higher magnitude than the streamwise energy $E^\dagger_{uu}$ as well as a different spatial distribution. In Figs. 11(e) and 11(f), the spatial distribution of lift-up production I_2 and converging-diverging production term I_4 are shown, respectively. The distribution of I_2 shows a strong similarity to that of E_{uu}, where I_4 is spatially consistent with E_{vv}. This indicates that the streamwise perturbation is driven mainly by the lift-up mechanism and the lateral perturbation is driven by the converging-diverging mechanism.

Figure 12 describes the volume-integrated production and dissipation at $\beta = 5$. These integrated quantities look quite similar to those from the two-dimensional mode at $\beta = 0$. The lift-up production I_2 and converging-diverging production I_4 are the primary and secondary production terms, respectively. It suggests that the lift-up mechanism and converging-diverging mechanism play an important role in the three-dimensional instability.

Based on the information from the direct and adjoint modes, the spatial sensitivity analysis at $\beta = 5$ is calculated using Eq. (17). The distribution in Fig. 13 suggests two origins sensitive to local perturbations: one from the shear of mean velocity and the other located in the wake. This is qualitatively similar to the observation at $\beta = 0$ (Fig. 9). In addition, the sensitive region also follows the trend of red streamlines from the base flow approximately.

V. THREE-DIMENSIONAL NUMERICAL SIMULATION

Results from numerical simulations are presented in this section to further reveal instability mechanisms in the transitional process. Furthermore, the instability mechanisms detected in the stability analysis are expected to have corresponding findings in the numerical simulation. The first step is to examine the macroscopic quantities. Figure 14 shows volume-averaged macroscopic

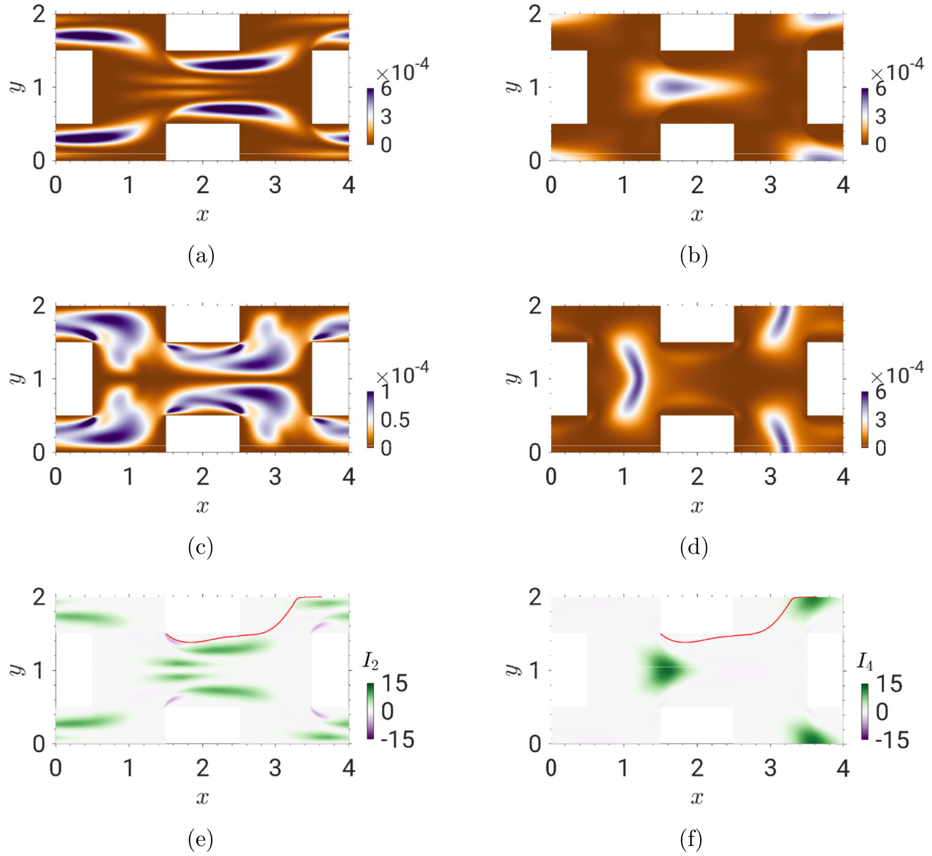

FIG. 11. Perturbation kinetic energy distribution of leading direct mode and adjoint mode at $\beta = 5$ from Re = 90 on the plane $z = 0$. (a) Kinetic energy in streamwise direction, E_{uu}. (b) Kinetic energy in lateral direction, E_{vv}. (c) Kinetic energy in streamwise direction, $E^{\dagger}_{uu}$. (d) Kinetic energy in lateral direction, $E^{\dagger}_{vv}$. (e) Production term I_2. (f) Production term I_4.

fluctuation energy from the numerical simulation, where $k = \frac{1}{2}(\langle\overline{U'U'}\rangle + \langle\overline{V'V'}\rangle + \langle\overline{W'W'}\rangle)$. The first Reynolds number observed with unsteady velocity fluctuation is Re = 90, whose fluctuation signal is however marginal. In the linear stability analysis, Re = 90 is the first Reynolds number with a growth rate above zero (Fig. 3). However, the growth rate is just slightly above zero ($\sigma = 0.05611$). In the numerical simulation, the most rapid fluctuation energy growth between Re = 90 and Re = 130 appears in the streamwise direction $\langle\overline{U'U'}\rangle$, followed by $\langle\overline{V'V'}\rangle$ and then $\langle\overline{W'W'}\rangle$. The $\langle\overline{U'U'}\rangle$ and $\langle\overline{V'V'}\rangle$ follow an approximate linear slope until Re = 130.

Streamlines based on the instantaneous velocity vector $\boldsymbol{U}$ on the x-normal cutting plane are given in Fig. 15. The cutting plane position is chosen to be $x = 0.9$ to demonstrate the evolution of instability from the recirculation region. The four panels include three stable Reynolds numbers Re = 50, Re = 60, Re = 90 (minor unstable) and the first significantly unstable Reynolds number Re = 100. A cold to warm color map is used with the absolute lateral velocity $|V|$. At Re = 50, no flow pattern on the y-z plane is captured by the streamlines. The flow shows a homogeneous distribution in the spanwise direction. This starts to change for Reynolds number Re $\geqslant$ 60. The magnitude of lateral velocity $|V|$ shows a wavy distribution in the spanwise direction, although the flow stays steady. This lift-up effect results in mushroom-like streamwise vortex pairs, which are clearly depicted in Fig. 15(b). These counterrotating mushroom vortex pairs exhibit

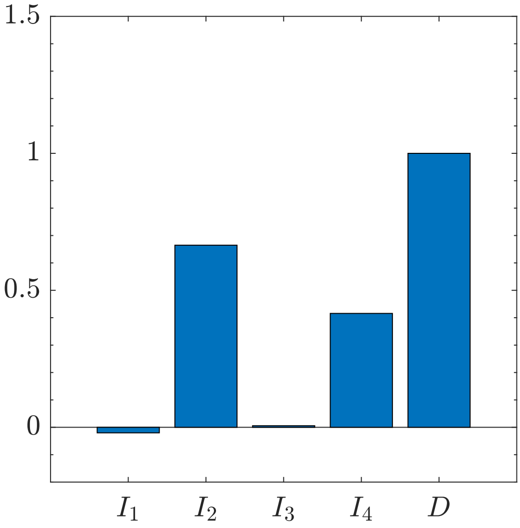

FIG. 12. Perturbation kinetic energy terms $\int I_i dV$, normalized by the dissipation $\int D dV$, at Re $= 90$.

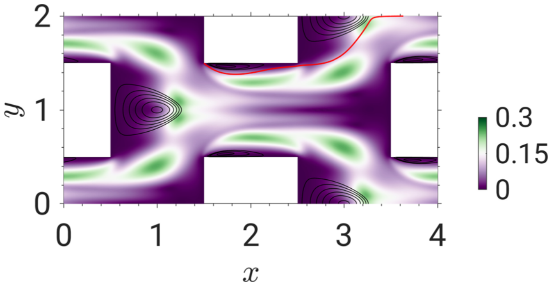

FIG. 13. Sensitivity analysis at $\beta = 5$ from Re $= 90$ on the plane $z = 0$.

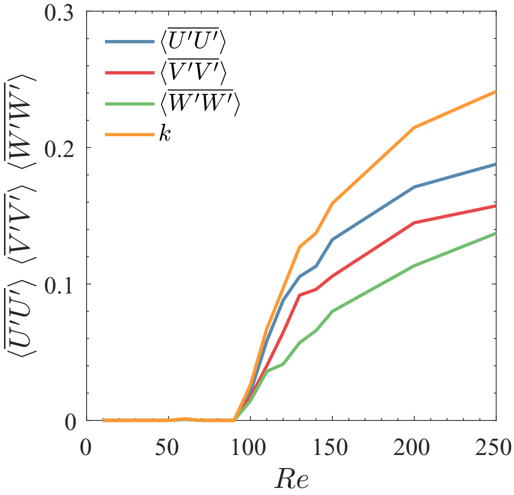

FIG. 14. Volume-averaged macroscopic fluctuation energy from the numerical simulations, where $k = \frac{1}{2}(\langle \overline{U'U'} \rangle + \langle \overline{V'V'} \rangle + \langle \overline{W'W'} \rangle)$.

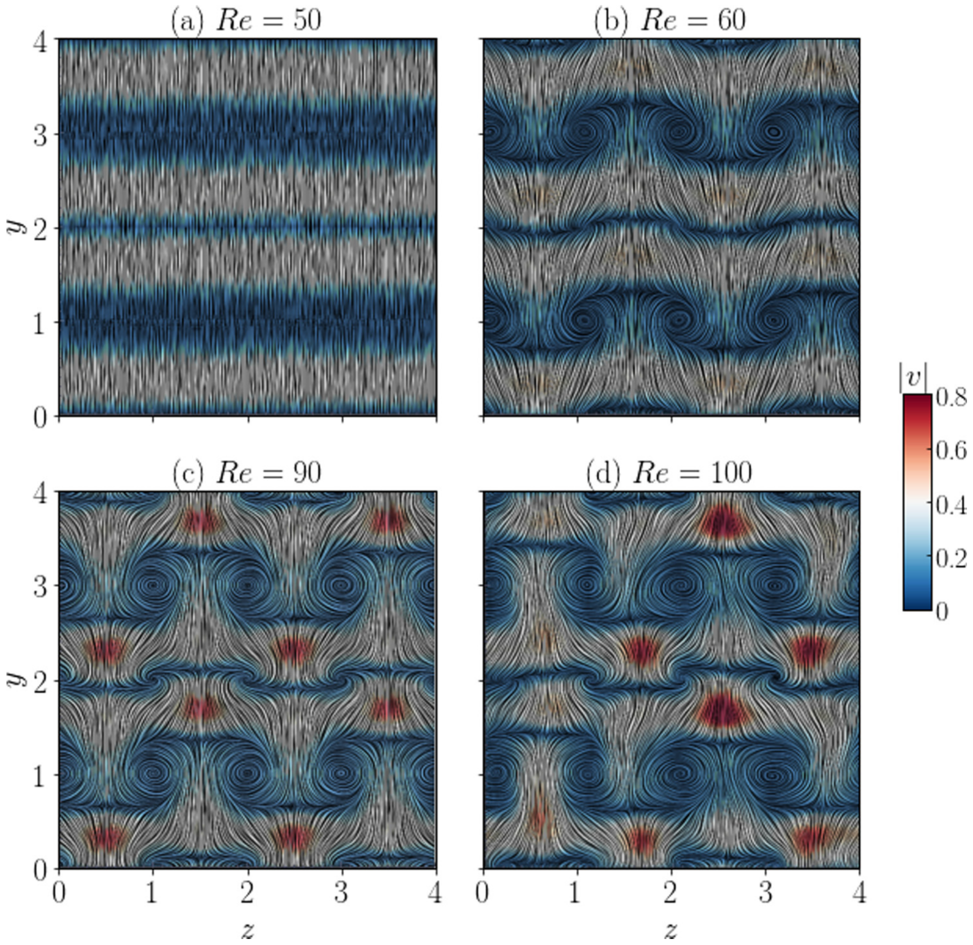

FIG. 15. Instantaneous streamlines on an $x = 0.9$ cutting plane, colored by the absolute lateral velocity $|V|$ for different Reynolds numbers.

a symmetry about the plane $z \approx 1.5, 3.5$ at this Reynolds number. The vortex core shows the lowest magnitude of lateral velocity, which is colored with the darkest tone. At $\mathrm{Re} = 90$, the inhomogeneous distribution of lateral velocity becomes very prominent. It drives the growth of mushroom vortices. The symmetry of counterrotating vortices breaks down at $\mathrm{Re} = 100$. However, the appearance of mushroom vortices is still clear and distinct. With increasing Reynolds number, these mushroom vortices become bluer and cannot be distinguished from chaotic structures with multiple frequencies. The spanwise wavelength of these vortices is $\lambda_{NS} \approx 2$, which indicates a wave number of $\beta_{NS} = 2\pi/\lambda_{NS} \approx \pi$. This is not far from the predicted three-dimensional instability at $\beta = 5$ in the stability analysis. Furthermore, the mode at wave number $\beta = \pi$ of the stability analysis shows a similar appearance to the one at $\beta = 5$.

To further visualize the three-dimensional spatial relationship of vortex instability, Fig. 16 shows streamwise vorticity contours $\omega_x = \pm 1.5$ colored with the lateral velocity V for the case $\mathrm{Re} = 90$. Two counterrotating vortex pairs are observed in one single streamwise channel. The demonstrated vortices spatially start from $x \approx 0.9$, which is in the same location as the streamwise cutting plane with mushroom vortices (Fig. 15). In other words, Fig. 15 describes the cutting plane on the heads of these streamwise vorticity contours. It ends at $x = 3.4$, which indicates a size over the pore scale $D = 2d$. It is interesting to notice that the heads of these vortices (in the negative x

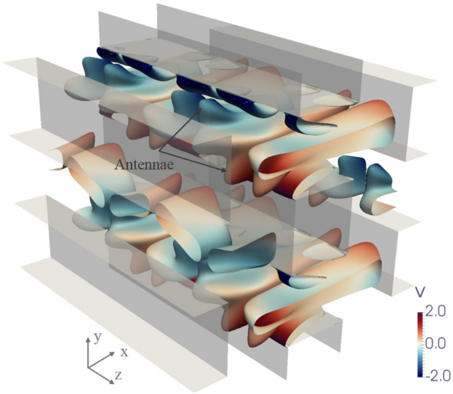

FIG. 16. Streamwise vorticity contour $\omega_x = \pm 1.5$, colored by lateral velocity V. Re $= 90$. A counterrotating pair consists of a positive contour $\omega_x = 1.5$ and a negative one $\omega_x = -1.5$, rotating against each other in the neighborhood.

direction) are located exactly at the centers of counterrotating mushroom vortices in Fig. 15. The vorticity contour exhibits most of its geometrical characteristics in the x-z plane, except for the two antennae in the positive and negative y direction. A pair of antennae have an approximate location of $(x, y) = (1.3, 2.8/3.2)$. Moreover, these antennae do not exist in the contours of $\omega_x = \pm 1.5$ at a lower Reynolds number Re $= 60$, although the mushroom vortices are observed at the same Reynolds number (Fig. 15). These vortices at Re $= 60$ show planar two-dimensional structures on the x-z plane, which is not demonstrated here for simplicity.

Figures 17(a) and 17(b) show spatial distribution of $\overline{U'U'}$ and $\overline{V'V'}$ at Re $= 100$ from numerical simulations. The streamwise component shows higher intensity than the lateral component, which is the same as indicated by the macroscopic quantity in Fig. 14. The spatial distributions of both $\overline{U'U'}$ and $\overline{V'V'}$ are very close to the unstable direct mode at $\beta = 5$ in Figs. 11(a) and 11(b), which suggests a consistency between linear stability analysis and numerical simulation.

Additional validation between the linear stability analysis and the numerical simulation requires a specially designed numerical simulation case. A numerical simulation case is conducted, which

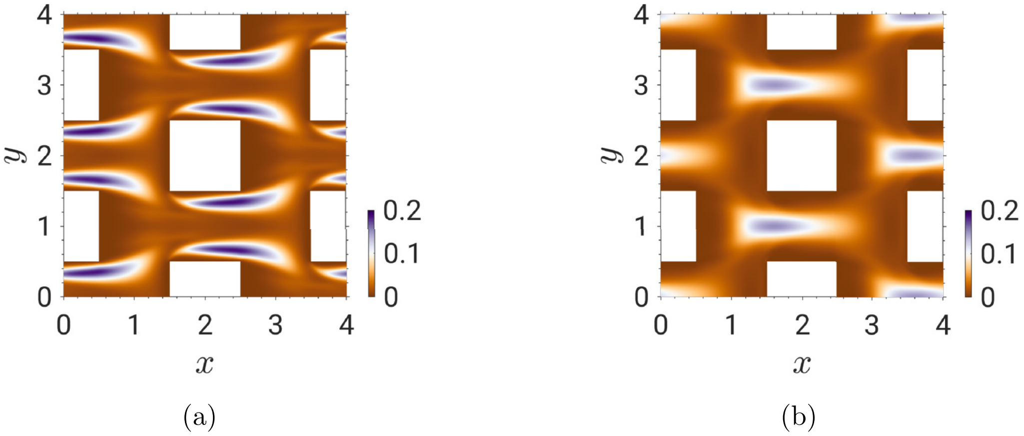

FIG. 17. Temporal and spatial average (in direction z) of streamwise and lateral fluctuation in the numerical simulation, Re $= 100$. (a) Streamwise fluctuation $\overline{U'U'}$. (b) Lateral fluctuation $\overline{V'V'}$.

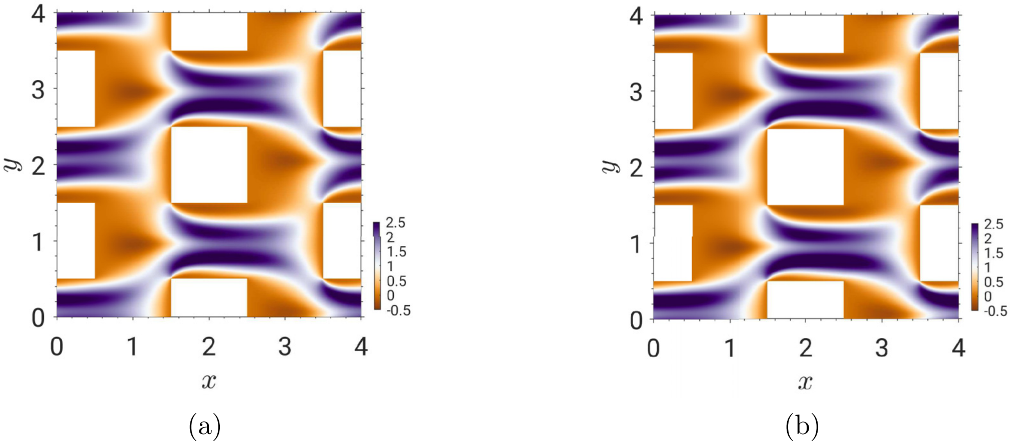

(a) (b)

FIG. 18. Velocity field U from the numerical simulation and reconstruction from LST. (a) Numerical simulation results of U at $\mathrm{Re} = 100$. (b) Reconstructed U from the mode at $\beta = \pi$ at $\mathrm{Re} = 100$.

starts from a subcritical Reynolds number ($\mathrm{Re} = 90$) with respect to the secondary oscillatory instability of the stationary periodic three-dimensional flow, to an unstable Reynolds number ($\mathrm{Re} = 100$). The slope of the evolution from the time signal obtained in the numerical simulation shows the information of growth rate. Probes are placed at multiple sensitive locations. The calculated growth rate is $\sigma_{NS} = 0.0482$, which is close to the prediction from the stability analysis ($\sigma = 0.053$ at $\beta = 3.3$).

The linear perturbed flow from Sec. IV D can be reconstructed by adding the base flow and the perturbation velocity field with a finite amplitude ($A\hat{\mathbf{u}}e^{\lambda t - i\beta z}$, $A = 40$) at the identical Reynolds number. The reconstructed field with the maximal amplitude is depicted as Fig. 18(b) with a comparison of the instantaneous numerical simulation field in Fig. 18(a). The constructed flow is based on the perturbation field from $\beta = \pi$, identical to the wave number of streamwise vortices in Fig. 15. The reconstructed field shows a qualitative similarity to the numerical simulation field. Both U fields tilt to the lower side and exhibit features of flow through sharp corners (dark purple colors).

In a series of numerical simulation cases, probe measurements are arranged at the sensitive locations in the domain. The first Reynolds number in the probe measurements showing fluctuations is $\mathrm{Re} = 90$, which agrees with the Reynolds number with the first bifurcation in the linear stability analysis. However, this signal is quite weak for making effective observations. We use the probe signal from the next simulated Reynolds number $\mathrm{Re} = 100$ to accomplish the observations. Figure 19(a) shows the temporal evolution of the streamwise velocity fluctuation U' and the associated Fourier spectrum in Fig. 19(b). The probe position $(x, y, z) = (1.7, 2.8, 2)$ is located at the convergent channel inlet as suggested by the global stability analysis. The periodicity of signals is evident with an overlap of different frequencies. In the Fourier spectrum, the observed strongest signal has a dominant circular frequency of $\omega_{NS} = 4.13$.

The critical Reynolds number from the stability analysis using the spanwise wave number $\beta = 2\pi/4 = 1.57$ ($L_z = 4$) is $\mathrm{Re}_{cr}^{LST}(\beta = 1.57) \approx 100$. An estimation of the critical Reynolds number can also be calculated from the numerical simulation. Following the Stuart-Landau model, which suggests that $A_f^2 \propto (\mathrm{Re} - \mathrm{Re}_{cr}^{NS})$ with A_f as the fluctuation amplitude, it is possible to extract the critical Reynolds number Re_{cr}^{NS} from the numerical simulation. This procedure is widely used in classical cases of stability analysis, such as the instability in the wake flow [45]. A_f^2 is obtained

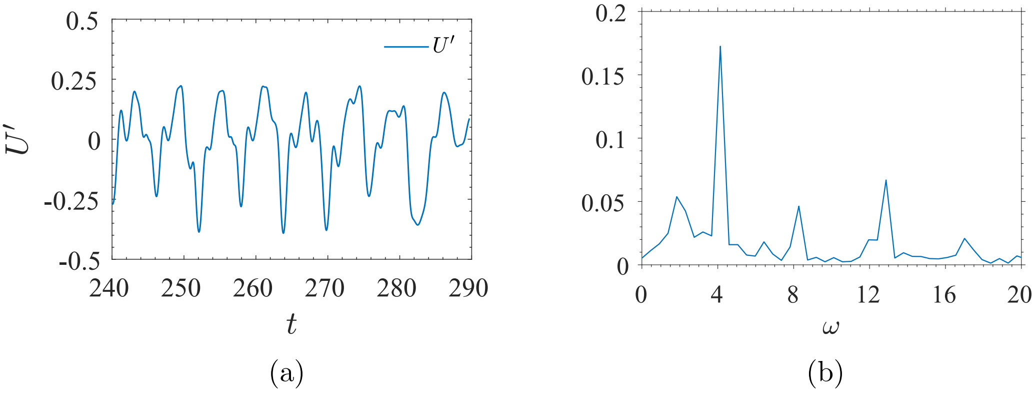

FIG. 19. Streamwise velocity fluctuation at Re = 100, at the location of $(x, y, z) = (1.7, 2.8, 2)$, where the instability at the channel entry occurs. (a) Probe measurement. (b) Power spectral density (PSD).

through integrating the dominant peak from the Fourier spectrum as in Fig. 19(b).

$$A_f^2 = \int_{f_c-\Delta f_l}^{f_c-\Delta f_u} \mathrm{PSD}(f)df. \tag{18}$$

Here f_c is the dominant peak frequency; Δf_l and Δf_u correspond to the interval of frequency around f_c, where the power spectral density (PSD) drops down to 15% of the peak value. Fitting the A_f^2 at different Reynolds numbers close to the criticality, the onset of fluctuations can be evaluated. Figure 20 depicts squared streamwise fluctuation amplitude u'^2_{fc} as a function of Reynolds number, based on the described procedure. This leads to the critical Reynolds numbers $\mathrm{Re}_{cr}^{NS} \approx 93$, which is close to the predicted critical Reynolds number from the linear stability analysis $[\mathrm{Re}_{cr}^{LST}(\beta = 1.57) \approx 100]$.

The instantaneous unsteady flow structures are depicted in Fig. 21. The instantaneous vortical structures at Re = 50, Re = 100, and Re = 150 are presented using the λ_2 criterion [46] colored with the instantaneous streamwise velocity field U. At Re = 50, only two-dimensional planar structures are captured at the inlet of the channel with contraction, as indicated by the streamlines in Fig. 15. On increasing Re to 100, complicated unsteady three-dimensional structures are found in the upstream of the channel inlet with a slight penetration into the streamwise channel. The heads of penetrations (in red color) appear in an approximately axis-symmetrical pair. The Reynolds number Re = 100 is the first significant unstable numerical simulation case. Further increasing the Reynolds number to 150, more unsteady turbulent structures are observed penetrating in the streamwise channels.

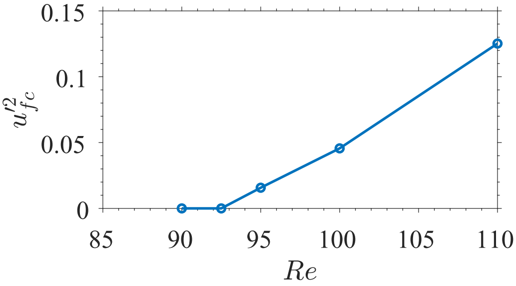

FIG. 20. u'^2_{fc} as a function of Reynolds number.

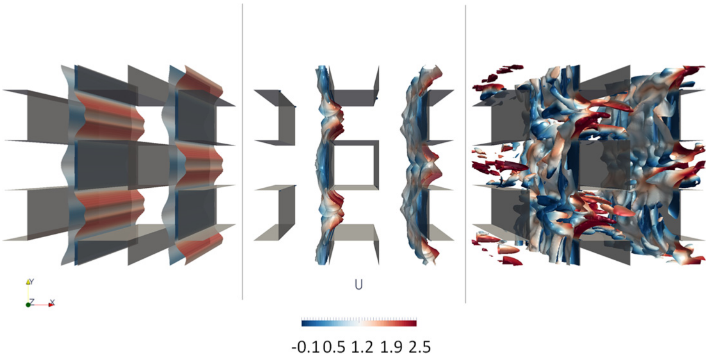

FIG. 21. Visualization of numerical simulation flow structures with threshold $\lambda_2 = -10$. Left to right: Re = 50, Re = 100, and Re = 150.

Based on the visual analysis in Fig. 21, these λ_2 visualizations illustrate the transitional process with the onset of instability in this porous medium. The origin of instability arises from the mushroom vortices in the area mixed with wake and diverging-converging patterns and results in counterrotating large-scale streamwise vortical pairs. This localized instability is well depicted by the λ_2 visualization in Fig. 21. And this instability is further transported downstream to the streamwise shear channel area as the Reynolds number increases (Re = 150). After that, the unsteady topology is similar to that of the fully developed turbulent flow observed in Chu *et al.* [14], where the turbulent structures are found mainly on the impinging surface and shear channel. The main difference is the significantly larger size of vortical structures here, which suggests a further breakdown of large vortices as the Reynolds number continuously increases. In addition, this similarity in the turbulence topology indicates that the transition process is accomplished after the streamwise channels are filled with unsteady flow structures. Further increasing the Reynolds number would not bring any paradigm shift of the flow status.

VI. SUMMARY AND CONCLUSIONS

Flow instability and the onset of transition in a porous medium are explained via global stability analysis and numerical simulation. The porous medium is presented by a REV with a specified morphology. In the numerical simulations, the REV is fully resolved with periodic boundary conditions in all three space directions and driven by a pressure gradient in one direction. In the stability analysis, a fine scan of spanwise wave number range $\beta = 0$–20 is used for all the considered Reynolds numbers to ensure the capture of all potentially unstable modes. The global stability analysis indicates two unstable modes as the Reynolds number progressively increases, a two-dimensional oscillatory one and a three-dimensional stationary one. Both modes exhibit comparable growth rates but the three-dimensional one is the most dangerous mode in most cases. The stability analysis shows the first unstable Reynolds number at Re = 90, where the leading growth rate at both $\beta = 0$ and $\beta = 5$ turns positive. A linear interpolation from the growth rate leads to a prediction of critical Reynolds number $\mathrm{Re}_{cr}^{LST} \approx 84$. Both instabilities ($\beta = 0$ and $\beta = 5$) have been discussed using the information from direct mode and adjoint mode. The energy analysis indicates that mainly the lift-up mechanism and converging-diverging mechanism create the instability and destabilize the flow.

In the numerical simulation, we observe mushroom vortices from Re = 60 onward, which corresponds to the stationary three-dimensional instability predicted by the stability analysis. These vortices can be explained by the lift-up mechanism and stay steady state until the critical Reynolds number is reached. At Re = 100 in numerical simulations, they lose the symmetry and significant fluctuation is captured by the probe measurement from the numerical simulation. The averaged

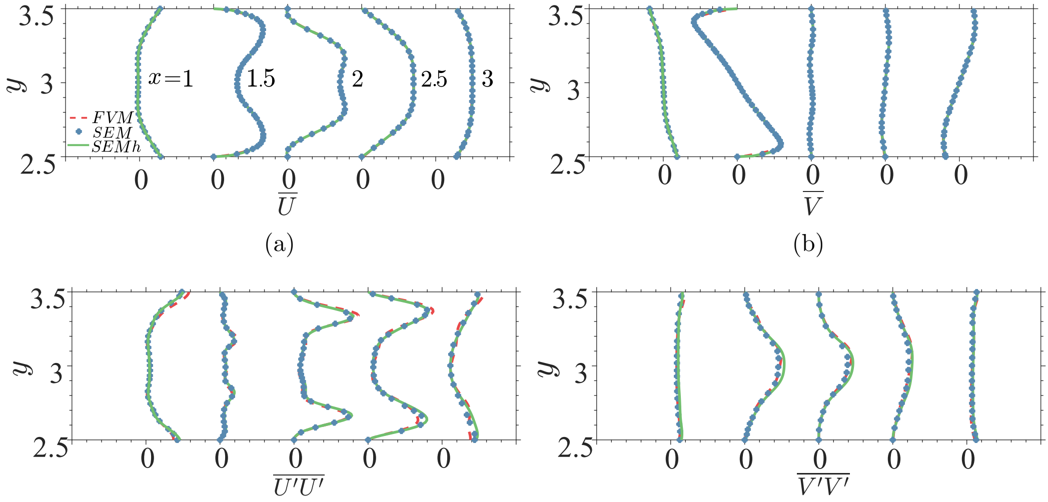

(a) (b)

(c) (d)

FIG. 22. Validation of the numerical simulation results FVM, SEM, and SEMh indicate the results at Re = 100, from FVM solver, SEM solver, and SEM solver with polynomial refinement, respectively. (a) Averaged streamwise velocity $\overline{U}$. (b) Averaged streamwise velocity $\overline{V}$. (c) Streamwise velocity fluctuation $\overline{U'U'}$. (d) Streamwise velocity fluctuation $\overline{V'V'}$.

streamwise $\overline{U'U'}$ and lateral velocity fluctuation $\overline{V'V'}$ at Re = 100 show strong similarity to the perturbation kinetic energy components at $\beta = 5$ from stability analysis, which confirms the prediction of unstable modes found in the numerical simulation.

ACKNOWLEDGMENTS

The published research is partly financed by MWK (Ministerium für Wissenschaft und Kunst) of Baden-Württemberg (Germany) as a part of the project DISS (Data-integrated Simulation Science). X.C. and B.W. are thankful to the Deutsche Forschungsgemeinschaft (German Research Foundation) for funding the project within SFB-1313 (Project No. 327154368). All the authors gratefully appreciate the access to the high performance computing facility Hazel Hen in HLRS, Stuttgart, Germany. The authors greatly appreciate the thoughtful comments and inspiration from the anonymous reviewers. We are also grateful for discussions with Dr. Visakh Vaikuntanathan.

APPENDIX

The numerical quality of the numerical simulation is examined by a cautious validation. Figure 22 shows the statistics from both finite-volume-method (FVM) and spectral-element-method (SEM) solvers at Re = 100. The applied spatial resolution is as introduced in Sec. III A. The results from the SEM solver are demonstrated with the basic polynomial setting of $P = 8$ and a polynomial refinement of $P = 11$. Five streamwise locations are chosen $x = 1$, 1.5, 2, 2.5, 3 between $y = 2.5$–3.5, which include areas with different flow phenomena. Averaged streamwise velocity $\overline{U}$, lateral velocity $\overline{V}$, and the corresponding velocity fluctuations $\overline{U'U'}$ and $\overline{V'V'}$ are shown in Fig. 22, panels (a), (b), (c), and (d), respectively. In all four groups of statistics, three numerical simulation alternatives show excellent agreement between each other. One should notice that the statistical convergence in transitional range requires significantly longer time for flow development and averaging than in the turbulent cases in Chu *et al.* [14]. This can be explained by the fact that the transitional flow is dominated by structures with low traveling velocity. Therefore, 50 flow-through times (L_x/U_{int}) have been used for developing the flow and another 50 flow-through times for sampling the quantities.

[1] B. Mayer, Investigations of pressure loss and heat transfer in regular metallic porous structures, Ph.D. thesis, University of Stuttgart, 2014.
[2] H. P. G. Darcy, *Les Fontaines publiques de la ville de Dijon: Exposition et application des principes à suivre et des formules à employer dans les questions de distribution d'eau, etc.* (V. Dalmont, Paris, 1856).
[3] A. Dybbs and R. V. Edwards, in *Fundamentals of Transport Phenomena in Porous Media* (Springer, Dordrecht, 1984), pp. 199–256.
[4] N. A. Horton and D. Pokrajac, Phys. Fluids **21**, 045104 (2009).
[5] R. J. Hill and D. L. Koch, J. Fluid Mech. **465**, 59 (2002).
[6] R. J. Hill and D. L. Koch, J. Fluid Mech. **453**, 315 (2002).
[7] D. L. Koch and R. J. Hill, Annu. Rev. Fluid Mech. **33**, 619 (2001).
[8] X. He, S. Apte, K. Schneider, and B. Kadoch, Phys. Rev. Fluids **3**, 084501 (2018).
[9] M. Agnaou, D. Lasseux, and A. Ahmadi, Comput. Fluids **136**, 67 (2016).
[10] Y. Jin, M.-F. Uth, A. V. Kuznetsov, and H. Herwig, J. Fluid Mech. **766**, 76 (2015).
[11] M.-F. Uth, Y. Jin, A. V. Kuznetsov, and H. Herwig, Phys. Fluids **28**, 065101 (2016).
[12] Y. Kuwata and K. Suga, Int. J. Heat Fluid Flow **55**, 143 (2015).
[13] K. Suga, Flow, Turbul. Combust. **96**, 717 (2016).
[14] X. Chu, B. Weigand, and V. Vaikuntanathan, Phys. Fluids **30**, 065102 (2018).
[15] V. A. Patil and J. A. Liburdy, Phys. Fluids **25**, 043304 (2013).
[16] F. Coletti, K. Muramatsu, D. Schiavazzi, C. J. Elkins, and J. K. Eaton, Phys. Fluids **26**, 055104 (2014).
[17] I. Lashgari, O. Tammisola, V. Citro, M. P. Juniper, and L. Brandt, J. Fluid Mech. **753**, 1 (2014).
[18] R. J. Poole, G. N. Rocha, and P. J. Oliveira, Comput. Fluids **93**, 91 (2014).
[19] J.-C. Loiseau, J.-C. Robinet, S. Cherubini, and E. Leriche, J. Fluid Mech. **760**, 175 (2014).
[20] F. Picella, J.-C. Loiseau, F. Lusseyran, J.-C. Robinet, S. Cherubini, and L. Pastur, J. Fluid Mech. **844**, 855 (2018).
[21] V. Theofilis, Annu. Rev. Fluid Mech. **43**, 319 (2011).
[22] P. G. Ledda, L. Siconolfi, F. Viola, F. Gallaire, and S. Camarri, Phys. Rev. Fluids **3**, 103901 (2018).
[23] O. T. Schmidt and U. Rist, J. Fluid Mech. **688**, 569 (2011).
[24] A. Fani, S. Camarri, and M. V. Salvetti, Phys. Fluids **24**, 084102 (2012).
[25] D. Lanzerstorfer and H. C. Kuhlmann, J. Fluid Mech. **702**, 378 (2012).
[26] O. Marquet, M. Lombardi, J.-M. Chomaz, D. Sipp, and L. Jacquin, J. Fluid Mech. **622**, 1 (2009).
[27] T. Ellingsen and E. Palm, Phys. Fluids **18**, 487 (1975).
[28] L. N. Trefethen, A. E. Trefethen, S. C. Reddy, and T. A. Driscoll, Science **261**, 578 (1993).
[29] J. Tchoufag, J. Magnaudet, and D. Fabre, Phys. Fluids **25**, 054108 (2013).
[30] S. Rapaka, S. Chen, R. J. Pawar, P. H. Stauffer, and D. Zhang, J. Fluid Mech. **609**, 285 (2008).
[31] P. Meliga, J. Chomaz, and D. Sipp, J. Fluids Struct. **25**, 601 (2009).
[32] E. Åkervik, L. Brandt, D. S. Henningson, J. Hoepffner, O. Marxen, and P. Schlatter, Phys. Fluids **18**, 068102 (2006).
[33] F. Giannetti and P. Luchini, J. Fluid Mech. **581**, 167 (2007).
[34] P. Luchini and A. Bottaro, Annu. Rev. Fluid Mech. **46**, 493 (2014).
[35] D. Barkley, H. M. Blackburn, and S. J. Sherwin, Int. J. Numer. Methods Fluids **57**, 1435 (2008).
[36] H. M. Blackburn, D. Barkley, and S. J. Sherwin, J. Fluid Mech. **603**, 271 (2008).
[37] See https://www.openfoam.org.
[38] C. D. Cantwell, S. J. Sherwin, R. M. Kirby, and P. H. Kelly, Comput. Fluids **43**, 23 (2011).
[39] C. D. Cantwell, D. Moxey, A. Comerford, A. Bolis, G. Rocco, G. Mengaldo, D. De Grazia, S. Yakovlev, J.-E. Lombard, D. Ekelschot *et al.*, Comput. Phys. Commun. **192**, 205 (2015).

[40] G. Karniadakis and S. Sherwin, *Spectral/hp Element Methods for Computational Fluid Dynamics* (Oxford University Press, 2013).

[41] S. Bagheri, E. Åkervik, L. Brandt, and D. S. Henningson, AIAA J. **47**, 1057 (2009).

[42] S. J. Sherwin and H. M. Blackburn, J. Fluid Mech. **533**, 297 (2005).

[43] G. J. Chandler, M. P. Juniper, J. W. Nichols, and P. J. Schmid, J. Comput. Phys. **231**, 1900 (2012).

[44] S. W. Gepner and J. M. Floryan, J. Fluid Mech. **807**, 167 (2016).

[45] P. Bohorquez, E. Sanmiguel-Rojas, A. Sevilla, J. Jiménez-González, and C. Martínez-Bazán, J. Fluid Mech. **676**, 110 (2011).

[46] J. H. Jeong and F. Hussain, J. Fluid Mech. **285**, 69 (1995).